

Beam halo measurements for special bunches in a storage ring by using a coronagraph

Cite as: Rev. Sci. Instrum. **92**, 123302 (2021); <https://doi.org/10.1063/5.0048318>

Submitted: 22 February 2021 • Accepted: 30 November 2021 • Published Online: 17 December 2021

 Ji-Gwang Hwang,  Gregor Schiwietz,  Paul Goslawski, et al.



View Online



Export Citation



CrossMark

ARTICLES YOU MAY BE INTERESTED IN

[Synchronized beamline at FLASH2 based on high-order harmonic generation for two-color dynamics studies](#)



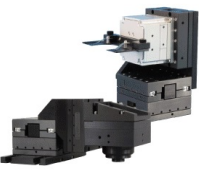
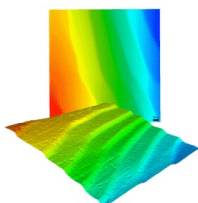
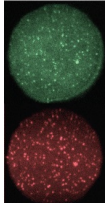
Review of Scientific Instruments **92**, 123004 (2021); <https://doi.org/10.1063/5.0063225>

[TrapREMI: A reaction microscope inside an electrostatic ion beam trap](#)

Review of Scientific Instruments **92**, 123201 (2021); <https://doi.org/10.1063/5.0065454>

[High-current \$H_2^+\$ beams from a filament-driven multicusp ion source](#)

Review of Scientific Instruments **92**, 123301 (2021); <https://doi.org/10.1063/5.0063301>

 MCL MAD CITY LABS INC. www.madcitylabs.com	<p>Nanopositioning Systems</p> 	<p>Modular Motion Control</p> 	<p>AFM and NSOM Instruments</p> 	<p>Single Molecule Microscopes</p> 
---	--	--	---	--

Beam halo measurements for special bunches in a storage ring by using a coronagraph

Cite as: Rev. Sci. Instrum. 92, 123302 (2021); doi: 10.1063/5.0048318

Submitted: 22 February 2021 • Accepted: 30 November 2021 •

Published Online: 17 December 2021



Ji-Gwang Hwang,^{a)} Gregor Schiwietz,^{a)} Paul Goslawski, and Markus Ries

AFFILIATIONS

Helmholtz-Zentrum Berlin (HZB), Albert-Einstein Straße 15, Berlin 12489, Germany

^{a)}Authors to whom correspondence should be addressed: ji-gwang.hwang@helmholtz-berlin.de and chiwietz@helmholtz-berlin.de

ABSTRACT

We demonstrate an experimental methodology for measuring the halo distribution of special bunches in a storage ring using a synchrotron radiation coronagraph composed of the objective lens and a re-diffraction system. The optimum parameters for the coronagraph were investigated within several boundary conditions by applying a paraxial Fourier transformation sequentially from one plane to the next plane. In addition, the effect of Mie-scattering was estimated for different polishing-quality lenses and it shows that a high-quality lens is capable of achieving a dynamic range of the monitor of about 10^4 . The capability of the halo monitor has been demonstrated by measuring the horizontal particle distribution of special bunches in beam experiments at the BESSY II storage ring. This monitor offers a new opportunity for continuous monitoring of special bunches in the storage ring such as transverse resonance island buckets and pulse-picking by resonant excitation, which open new horizons for storage rings that are capable of sophisticated experiments using a single bunch signal as well as serving high-flux users simultaneously.

© 2021 Author(s). All article content, except where otherwise noted, is licensed under a Creative Commons Attribution (CC BY) license (<http://creativecommons.org/licenses/by/4.0/>). <https://doi.org/10.1063/5.0048318>

I. INTRODUCTION

In future high power accelerators, such as MHz-repetition-rate x-ray free-electron lasers (FEL),^{1–7} energy recovery linacs (ERL),^{8–15} heavy-ion accelerators,^{16–23} and particle colliders^{24–33} are indispensable tools for fundamental and applied sciences. It is crucial to understand the mechanisms that lead to halo formation, resulting in uncontrolled beam losses. The beam losses, in turn, lead to reduced machine availability for users and it may become very costly owing to activation or damage of accelerator components. A halo monitor is one of the most crucial diagnostics for these high power accelerators to analyze uncontrolled beam losses in the machine.³⁴ For instance, in the case of the energy recovery linear demonstrator bERLinPro,³⁵ the multi-particle tracking simulation using the OPAL code,³⁶ which can compute relativistic particle distributions in full six-dimensional phase space taking into account space-charge forces with multiple-components, shows a halo-particle distribution above $6\sigma_y \approx 1.3$ mm with an integrated fractional power of roughly 10^{-3} .³⁷ Collimated bellows in a cryomodule of bERLinPro, however, cannot exceed a heat load of 50 W. This highlights uncontrolled beam losses due to halo particles, corresponding to 10^{-5} levels of the maximum beam power. By observing the halo distribution, we

can adjust beam optics to mitigate the halo intensity as well as get rid of the halo particles by dedicated high-power beam collimators to prevent damages to the machine. Furthermore, the halo monitor enables the non-invasive measurements of special bunches in a storage ring. One example is the transverse resonance island buckets (TRIBs) method,^{38,39} where a few bunches are stored on a displaced orbit. Another example is the production of a blurred bunch for quasi-single bunch experiments using a method of pulse-picking by resonant excitation (PPRE).⁴⁰ Both methods open new horizons for storage rings to serve timing users without invading the availability for high-flux users. This demands beam diagnostics with a dynamic range of the monitor of about 10^4 .

Various techniques for transverse profile measurements of beams in accelerators have been developed.^{41–49} However, these are fundamentally limited to the dynamic range of about two orders of magnitude at the final image acquisition. The limitation is due to the operation range of detectors as well as the background produced by the diffraction or scattering from optical components. We refer to both sources of the background produced by diffraction simply as background light in this paper. For the observation of the halo distribution with the contrast of below 10^{-4} to the beam core, the dynamic range of monitors needs to be high,

being able to cover at least four orders of magnitude in intensity changes. For this purpose, many special instruments and technologies such as coronagraphs,^{50–53} wire-scanners,^{54,55} sophisticated phosphor screens,^{56–58} diamond detectors,⁵⁹ innovative camera systems based on charge injection devices,^{60,61} and optical masks using a digital micromirror device (DMD)⁶² have been devised, demonstrated experimentally, and utilized. Particularly, the coronagraph offers the observation of full 2-D halo distribution without any disturbance to the primary beam and it has already been demonstrated at the KEK Photon Factory as well as CERN to achieve a 6×10^{-7} ratio for the background to peak intensity.

In this paper, we study the theoretical interpretation of the optical system of the coronagraph halo monitor. Here, we investigate the influence of the focal length and quality of lenses by applying Fourier optics.⁶³ This approach provides insight into the effect of Mie-scattering by digs distributed on the surface of an objective lens and the optical system of the coronagraph for suppressing background light produced by input disturbance. The performance of the designed coronagraph is verified experimentally for various operation modes at the BESSY II storage ring.

II. CORONAGRAPH BASED HALO MONITOR

The schematic layout of the coronagraph is shown in Fig. 1. The coronagraph-based halo monitor comprises

- an objective lens (first lens) to produce a real beam image with an attached entrance pupil,
- baffle slits to suppress stray light in the entrance light path,
- an opaque element (square shape) at image plane A to block a high-intensity image core,
- a field lens (second lens) slightly behind the image plane A to produce well-defined re-diffraction fringes,
- the so-called Lyot stop (to be discussed later), and
- a relay lens (third lens) to form the filtered image of the beam on the charge-coupled device (CCD) camera sensor surface.

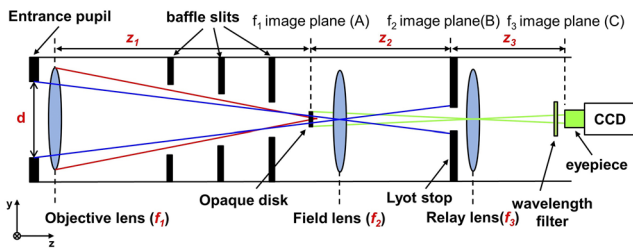


FIG. 1. Schematic layout of the coronagraph comprised an objective lens (first lens) with a focal length of f_1 , baffle slits, opaque element, field lens (second lens) with a focal length of f_2 , Lyot stop (diaphragm), and relay lens (third lens) with a focal length of f_3 . Planes A and C denote the image planes of the objective and relay lenses, respectively, and plane B represents the image plane of the field lens. The outer diameter of the entrance pupil (square shaped) is d and z_1 , z_2 , and z_3 denote the distance between the objective lens and plane A, planes A to B, and planes B to C, respectively. The red, blue, and green lines represent images formed by the objective lens (beam image), field lens (entrance pupil image), and relay lens (the image of plane A), respectively.

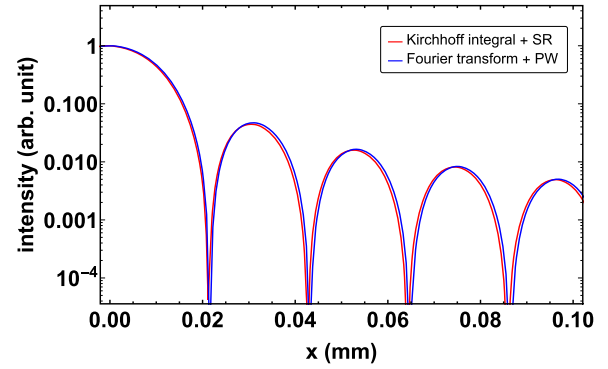


FIG. 2. Diffraction fringes as a function of the lateral distance computed numerically by the integral in Eq. (2) with synchrotron radiation properties (red) and Fourier optics with a plane wave (blue) on the image plane of the objective lens with a distance from the source point to the entrance pupil of 13.5 m, a focal length of 1 m, a wavelength of 500 nm, and a diameter of the entrance pupil of $d = 25$ mm. The x-scale of the Fourier optics result has been rescaled by $z_0/(f_1 - z_0) = 1.08$ to account for the finite distance of the source point.

We assumed that the distances between all beam-blocking elements (entrance pupil, opaque element, Lyot stop) and corresponding lenses are effectively zero. This type of monitor adopts the so-called re-diffraction optics to mitigate the background structures due to the diffraction fringes generated by the finite aperture at the entrance pupil. The position-dependent light intensity (see diffraction fringes in Fig. 2) of these structures amounts to about 1% of the central high-intensity light. Therefore, optical diagnostics such as direct source size monitors and pinhole cameras are not able to measure the halo distribution far away from the center. Lyot's idea for the coronagraph, which has a field lens at the image plane of the objective lens and places an outer mask (Lyot stop) at the image plane of the field lens to remove the majority of lower-order diffraction fringes produced by the re-diffraction optics, can reduce the background light by at least two orders of magnitude.^{50–52}

A. Theoretical interpretation

The scalar wavefront at the entrance pupil is represented by its complex amplitude $\Psi_{input}(x, y)$ and it is driven by the profile of synchrotron radiation. The distribution of electric fields at the image plane (x_A, y_A, z_A) produced by an objective lens with a finite aperture can be represented by applying the simplified Kirchhoff integral theory (without obliquity effects) including action of a lens as⁶⁴

$$\Psi_A(x_A, y_A, z_A) = \frac{1}{i\lambda} \iint dxdy \Psi_{input}(x, y) \phi_{lens}(x, y) \frac{e^{ikr_A}}{r_A}, \quad (1)$$

$$= \frac{1}{i\lambda} \iint dxdy \Psi_{input}(x, y) e^{-i\pi \frac{x^2 + y^2}{\lambda f}} \frac{e^{ikr_A}}{r_A}, \quad (2)$$

where $\Psi_{input}(x, y) = (E_{0\sigma} + E_{0\pi})e^{i\Phi(x)}$ is the synchrotron radiation field, x and y are transverse coordinates at the entrance pupil, $k = 2\pi/\lambda$, f is the focal length of the lens, and $r_A = \sqrt{(x - x_A)^2 + (y - y_A)^2 + L^2}$, where the distance from the lens to the image is $L = fz_0/(z_0 - f)$ and z_0 denotes the distance from the source point to the entrance pupil. The electric fields of σ^- and π^-

components and the phase of synchrotron radiation are given by⁶⁵

$$\begin{aligned} E_{0\sigma} &= \frac{4\pi e\gamma}{z_0 c} \sqrt{\Lambda} Ai'(\Lambda(1 + \gamma^2(y/z_0)^2)), \\ E_{0\pi} &= \frac{4\pi e\gamma}{z_0 c} \Lambda(y/z_0) Ai(\Lambda(1 + \gamma^2(y/z_0)^2)), \\ \Phi(\vec{x}) &= \frac{2\pi z_0}{\lambda} (1 - R^2/(8z_0^2\gamma^4)) \\ &\quad + \frac{\pi z_0}{\lambda} \left((x/z_0 + R/(2z_0\gamma^2))^2 + (y/z_0)^2 \right) \\ &\quad + \frac{\pi R}{\lambda} \left(\frac{1}{3} (x/z_0)^3 + (x/z_0)(y/z_0)^2 \right), \end{aligned} \quad (3)$$

where $\Lambda = (\pi R/(\lambda\gamma^3))^{2/3}$, R is the electron orbit radius, c is the speed of light, e is the elementary charge, γ is the Lorentz factor, and $Ai(x)$ and $Ai'(x)$ are the Airy function and its derivative. This indicates that the electric field and phase of synchrotron radiation depend on the beam energy, the distance from the source point, and the wavelength, resulting in the wavelength-dependent angular width. To identify the distribution of diffraction patterns at the image plane of the objective lens, the calculation was performed for σ^- polarized light by using the integral in Eq. (2) and the complex synchrotron radiation amplitude as defined by Eq. (3). The result has been compared with the numerical computation by Fourier optics with an initial plane wave. The parameters such as the distance from the source point to the entrance pupil of 13.5 m and the central wavelength of $\lambda = 500$ nm are used. As shown in Fig. 2, the diffraction fringes on the image plane of the objective lens calculated by Fourier optics with a plane wave quantitatively agree well with the result calculated by the integral in Eq. (2) taking into account synchrotron radiation properties in Eq. (3). This is no surprise because the small ratio of d/z_0 selects a flat part of the synchrotron radiation angular distribution and this wave front is close to a plane wave at $\lambda = 500$ nm. Consequently, the wave in the image plane can be approximated to the Fourier transform of the plane wave at its entrance. This is equivalent to the classical optics approach using Fourier transforms, in which the waveform is regarded to be made up of a superposition of plane waves. The complex amplitude at the image plane of the objective lens (A) can be expressed as⁶⁶

$$\Psi_A(x_A, y_A) = \frac{\phi_{z1}}{i\lambda z_1} \mathcal{F}_{\lambda z_1} [\Psi_{input}(x, y) \times \mathcal{P}_{input}(x, y)], \quad (4)$$

where $\mathcal{F}_{\lambda z}$ denotes the 2D Fourier transformation with spatial frequencies of $x/(\lambda z)$ and $y/(\lambda z)$, $\mathcal{P}_{input}(x, y)$ represents the transmission function at the entrance pupil, $\phi_z(x, y) = \exp[i\pi(x^2 + y^2)/(\lambda z)]$, and z_1 is the distance from the entrance pupil to the image plane of the objective lens. The squared modulus of the complex amplitude, $|\Psi|^2$, is a real number interpreted as the intensity of the light. The quadratic phase term in front of the Fourier transform is canceled when computing the intensity. It is expressed for each optical element as a sequence of functions of the preceding complex amplitude and transmission function. For each step, we assume that the entrance pupil or the obstacle at an image plane is very close to the corresponding subsequent focusing lens. Hence, considering the coordinates (x_A, y_A) at plane A and (x_B, y_B) at plane B, the complex amplitude at the image plane of the field lens with Fresnel integral⁶³

to propagate the image on the entrance pupil to plane B becomes

$$\begin{aligned} \Psi_B(x_B, y_B) &= \frac{\phi_{z2}}{i\lambda z_2} \iint dx_A dy_A \Psi_A \mathcal{P}_A \\ &\quad \times e^{i\frac{\pi}{\lambda} \left(\frac{1}{z_2} - \frac{1}{f_2} \right) (x_A^2 + y_A^2)} e^{-i\frac{2\pi}{\lambda z_2} (x_B x_A + y_B y_A)}, \end{aligned} \quad (5)$$

where z_2 is the distance from plane A to B and \mathcal{P}_A is the transmission function at plane A considering the opaque element. The three quadratic phase factors ϕ_{z1} , ϕ_{z2} , and ϕ_{f2} cancel each other since it satisfies the $\frac{1}{z_1} + \frac{1}{z_2} - \frac{1}{f_2} = 0$ condition at the image plane of the field lens. Then, the complex amplitude at the plane B is given by

$$\Psi_B = \frac{-\phi_{z2}}{\lambda^2 z_1 z_2} \mathcal{F}_{\lambda z_2} [\tilde{\Psi}_A \times \mathcal{P}_A], \quad (6)$$

where $\tilde{\Psi}_A = \mathcal{F}_{\lambda z_1} [\Psi_{input} \times \mathcal{P}_{input}]$. The relay lens shapes the light beam and opaque element images of plane A on plane C. Considering the coordinates (x_C, y_C) at plane C, the transmission function at plane B \mathcal{P}_B , and based on the same principle as discussed in Eq. (6), the wave front in plane C is obtained by performing Fourier transformation of $\Psi_B \times \mathcal{P}_B$,

$$\Psi_C(x_C, y_C) = -\frac{\phi_{z3}}{\lambda^2 z_1 z_2} \mathcal{F}_{\lambda z_3} [\tilde{\Psi}_B \times \mathcal{P}_B], \quad (7)$$

where $\tilde{\Psi}_B = \mathcal{F}_{\lambda z_2} [\tilde{\Psi}_A \times \mathcal{P}_A]$. As described by Eqs. (2)–(7), the light propagation inside the coronagraph can be calculated by applying a paraxial Fourier transformation sequentially from one plane to the next plane using Fourier optics.^{50,63}

Using Eq. (4), the beam distribution and diffraction fringe at the image plane of the objective lens are calculated with a beam size of $\sigma_x = 105 \mu\text{m}$, a magnification M of 1/12.5, a wavelength of 500 nm, an entrance pupil size d of 25 mm, and a focal length of 1 m. The re-diffraction system has a field lens near the image plane of the objective lens. Since the field lens forms the image of the entrance pupil onto the image plane of the lens, the diffraction fringe shown in Fig. 3 is re-distributed near the geometrical image of the aperture edge of the entrance pupil, and the position and magnitude of the peak intensity at plane B are determined by $d \times z_1/z_2$. In order to estimate the effect of the focal length of the field lens, the intensity distribution on the image plane of the field lens is calculated with a plane wave as a function of the focal length using Babinet's theory,⁶³ in which the diffraction pattern from an opaque element is identical to that from a hole of the same size and shape except for the overall forward beam intensity.⁵⁰ The influence of the aperture of the field lens and the opaque element is taken into account in the calculation.

As shown in Fig. 4, when the focal length of the field lens increases, the distance between two peaks, which is corresponding to the edge of the entrance pupil, is widened by the ratio of the focal length of the objective and field lenses, $d \times z_1/z_2$. In addition, this allows the background light to be spread over a wider space, which is suitable to remove the background light effectively by adjusting the Lyot stop. This wider space is necessary because the mechanism of the iris aperture for the Lyot stop involves a fixed uncertainty for the size of the opening. The two peaks are separated sufficiently at the Lyot stop and the power within the opening of the Lyot stop is feasible for observing halo particles at the level of 10^{-5} when f_2/f_1 is $\geq 1/2$. Since the intensity on the image plane strongly depends on the opening of the Lyot stop, it should be finely adjustable. The a squared Lyot

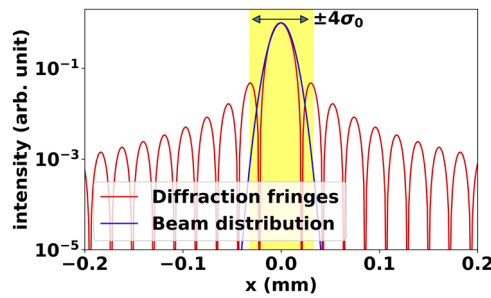


FIG. 3. Beam distribution and diffraction fringes at the image plane of the objective lens $|\Psi_A|^2$ with a beam size of $\sigma_x = 105 \mu\text{m}$, a magnification of $1/12.5$, a wavelength of 500 nm , a diameter of the entrance pupil of 25 mm , and a focal length of 1 m . The x-scale of the Fourier optics result has been rescaled by $z_0/(f_1 - z_0) = 1.08$ to account for the finite distance of the source point.

stop rotated by 45° or a circular-type Lyot stop is appropriate to prevent the invasion of the power from the corner of the re-diffraction fringes, which contains the maximum power. The 2D intensity distribution at the position of the Lyot stop with a focal length of 0.5 m is shown in Fig. 5.

The diffraction fringes created in the third stage, the relay system, can be calculated using the Fourier transform with the Lyot stop as an entrance pupil on the image point of the relay lens as given in Eq. (7). At this stage, the intensity of the light is already reduced to the level of 10^{-4} , so the unwanted signal generated by diffraction is negligible. The outer diameter of the relay-system tube is set to 50 mm and the opening of the Lyot stop is adjustable up to 20 mm . Since the transverse magnification of the relay system is not enough, an additional projection lens (eyepiece) in the front of the CCD camera is also considered to enlarge the image by an order of magnitude. The intensity distribution of the diffraction pattern on the imaging plane of the relay lens is calculated with a radius of the Lyot stop (r_{Lyot}) of 5 mm .

As shown in Fig. 6, the background light of the designed set-up with 1 m objective lens, 0.5 m field lens, 0.25 m relay lens, and a radius of the Lyot stop of 5 mm is about 3.0×10^{-5} , which is sufficient to observe the special bunches with significantly larger widths or at

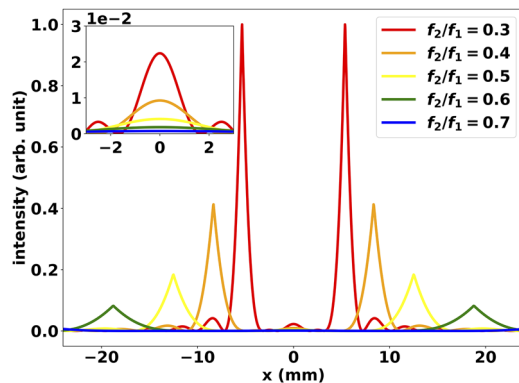


FIG. 4. Intensity distribution at the image plane of the field lens $|\Psi_B|^2$ with various focal lengths including a diameter of the entrance pupil of 25 mm , a focal length of the objective lens of 1 m , and a size of an opaque element of $8 \times \sigma_0 = 8 \times \sigma_x \times M$.

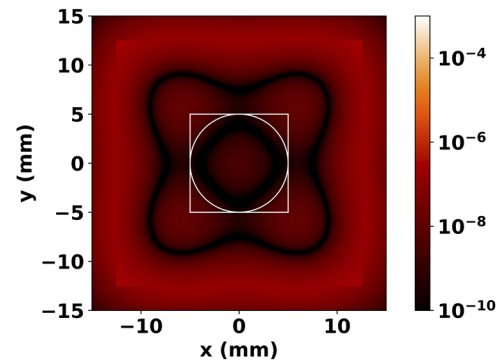


FIG. 5. Log-scale 2D intensity distribution profile on the image plane of the re-diffraction system $|\Psi_B|^2$ with a 1 m focal-length objective lens and 0.5 m focal-length field lens. White solid lines denote the two different types of the Lyot stop. A circular collimator is more efficient to reject the background light due to the sharp square edges (related to all deviations from the central cylindrical symmetry) and mitigate the effect of a misalignment of the Lyot stop.

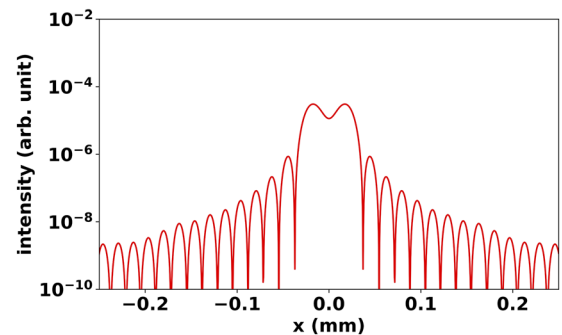
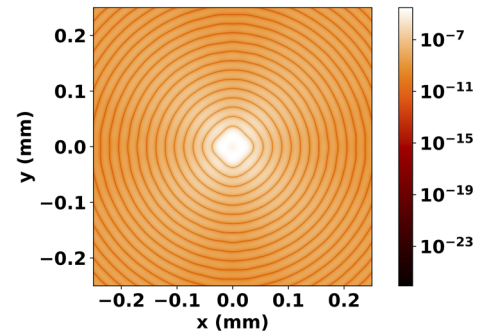


FIG. 6. Intensity distribution of the diffraction pattern on the image plane of relay lens $|\Psi_C|^2$ with a radius of the Lyot stop of 5 mm .

lateral positions further away from the central orbit in a storage ring (Tables I and II).

B. Background light by Mie scattering

At such a low signal level, it is necessary to take into account Mie scattering⁶⁷ from the digs and scratches on the surface of the objective lens since Mie scattering has a strong angular dependency of the scattered intensity, especially for smaller particles and it is much stronger than Rayleigh scattering and, therefore, a potential

TABLE I. Dimensions and shapes of the disturbances used in simulations for the coronagraph.

Type	Diameter (mm)	Shape
Entrance pupil	25 × 25	Square
Opaque element	8 × M × σ _x (~67 μm)	Square
Lyot stop	6	Circular
Aperture diameter	50	Circular

TABLE II. Lens specs.

Type	Focal length	Lens type (in experiments)	Quality
Objective lens	1000 mm (z ₁ ≈ 1 m)	Singlet (w/o coating)	≤10-5
Field lens	500 mm (z ₂ ≈ 1 m)	Achromatic doublet	40-20
Relay lens	250 mm (z ₃ ≈ 0.3 m)	Achromatic doublet	40-20

source of interference for this weaker light scattering process. The digs and scratches on the lens surface are inevitable during the manufacturing process. It introduces additional noise by Mie-scattering, which is elastically scattered light of particles when the size of the scattering particles is comparable to the wavelength of the light. The surface quality is widely represented by a “Scratch-Dig (S – D)” number that is an evaluation of the surface imperfections, such as scratches and pits, or digs. The scratch number denotes the maximum width allowance of a scratch as measured in micrometers and the dig number indicates the maximum diameter allowance for a dig in hundredths of a millimeter. Once all scratches and digs have been quantified, determining the number of allowable defects is required. This number satisfies the following conditions:⁶⁸

$$\sum L_{SN} < \phi/4, \quad (8a)$$

$$N = \phi/20, \quad (8b)$$

$$\sum d < 2ND, \quad (8c)$$

where ϕ is the diameter of the optical element, L_{SN} is the length of the scratch, N is the total number of allowable maximum size digs, d is the diameter of a dig, and D is the specified dig number. Equation (8a) represents that the sum of all scratch lengths with the specified scratch number will not exceed a quarter of the diameter of the optic. Equation (8b) means that the total number of allowable maximum size digs will not exceed the diameter divided by 20. Equation (8c) indicates that the sum of all dig diameters will be less than twice the total number of allowable maximum sized digs multiplied by the specified dig number. Then, the sum of the products of the scratch numbers times the ratio of their length to the diameter of the element cannot exceed half the maximum scratch number.

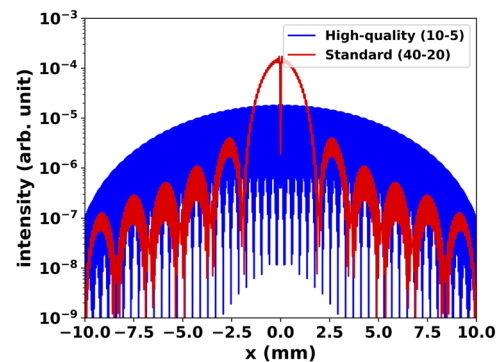
To achieve the background level below a contrast of 10^{-4} , the polishing quality of an objective lens should be qualified. For instance, it has been proven that the effect of Mie-scattering owing to the dig and scratch with a size of 200 μm (a dig number of 20) on the surface of the lens produces the background light of

3×10^{-4} .⁶⁹ Our numerical simulations are performed to estimate the required quality of the objective lens for achieving an intensity level lower than 10^{-4} contrast. The digs have a greater size than scratches in diameter and depth, and they are discontinuous, resulting in enhanced forward scattering and a wide distribution of back-ground light produced by the diffraction at the image plane of the objective lens. Scratches, however, produce a sharp noise distributed near the opaque element because they have a continuous distribution (forward scattering instead of diffuse scattering). Therefore, the opaque element can obstruct the noise from the scratches. In our Mie-scattering simulation, we decided to consider only the main effect, namely, the digs, which were treated as random disturbances at the entrance pupil. It was generated in accordance with the three conditions, Eqs. (8a), (8b), and (8c). The complex amplitude of the light diffracted by many digs on the surface of the objective lens at the image plane of the objective lens can be represented by

$$\Psi_A(x, y) = \frac{\phi_{z1}}{i\lambda z_1} \sum_j \mathcal{F}_{\lambda z_1} [P_j(r_j, x_j, y_j) e^{-i\frac{2\pi}{\lambda}((x_j-x)+(y_j-y))}], \quad (9)$$

where $P_j(r_j, x_j, y_j)$ denote the j th round shape dig on the lens surface located at (x_j, y_j) with a radius of r_j . $P_j(r_j, x_j, y_j)$ is a stochastic probability for having a dig at the position of (x_j, y_j) with a radius of r_j . Equation (9) describes the Mie simulation by adding phase kicks to the penetrating light. With the randomly distributed digs, the noise level at the image plane of the relay lens was simulated for standard quality (40-20) and high-quality (10-5) optical components regarding the disturbances in the beamline such as the apertures, the opaque element, and the Lyot stop. The total number of digs is only about 0.5 per cm² for the selected two cases and the calculation results are shown in Fig. 7.

The standard-quality lens has a higher and narrow peak noise in the center than the high-quality lens because the larger diameter digs produce the noise near the center with a narrow bandwidth at the final image plane. Moreover, the standard-quality lens has a larger number of digs than the high-quality lens so that superimposing the noise peaks forms the sharp and higher peak at the center. The background noise generated by Mie-scattering is partially suppressed by the standard Lyot stop opening in the re-diffraction optics. However, there is no gain in the signal-to-noise ratio by

**FIG. 7.** Simulated background light pattern at the image plane of the relay lens produced by Mie scattering at the objective lens for standard (red, 40-20) and high-quality (blue, 10-5) lenses.

reducing the opening of the Lyot stop further. In addition, the background noise produced by the digs is not suppressed when the digs are located near the center of the lens. Therefore, exquisite surface polishing near the center of the lens should be considered in order to measure the halo distribution at the level below a 10^{-5} contrast relative to the core intensity. In addition, the microroughness of the surface is also a significant parameter to mitigate the scattering of light on the surface.⁷⁰ In general, the pitch polishing of substrates could obtain 1–1.5 nm roughness, but the anti-reflection coating has the roughness of about 3 times worse than the roughness of the substrates. Therefore, uncoated optical lenses are inevitable to achieve the necessary surface quality as well as roughness requirements.

III. BEAM EXPERIMENTS AT BESSY II

A beam test is conducted at a diagnostics beamline of BESSY II that provides a multi-platform for research and development of various synchrotron radiation based monitors.^{71,72} The distance from the source point to the entrance pupil of the halo monitor is 13.5 ± 0.5 m. For this experiment, the focal lengths of the objective lens, the field lens, and relay lens are determined to be 1.0, 0.5, and 0.25 m, respectively, taking into account the available space for the installation of the monitor at our platform. The objective lens with a focal length of 1 m was manufactured for a high quality better than (10/5) without surface coating, especially to minimize the number of digs and scratches within the clear aperture, which corresponds to 1/2 of the aperture diameter. For the field and relay lenses, commercially available achromatic lenses with a diameter of 50 mm are adopted and all elements such as an entrance pupil, lenses, and baffle slits are installed in a reflection-free closed structure to prevent ambient light. As shown in Fig. 6, it is still possible to obtain the background light at the level of 10^{-4} with respect to the core intensity, which enables measurements of features of special bunches in a storage ring. The square entrance pupil with the opening of 25 mm was adopted. The bar-shaped opaque elements were printed by a 3D printer with an irregular reflection surface for various sizes from 150 to 580 μm with a fabrication error of 100 μm . A GT1920 CCD camera that has high linearity over extensive exposure time from 10 μs to 60 s is used in the experiments. Considering the bunch revolution times of 800 ns and the manifold of bunches per turn, the camera will always determine averaged light signals and a synchronization was not necessary.

The BESSY II storage ring has been providing a new bunch filling pattern in the top-up mode, namely, the standard user mode. This consists of a hybrid (chopper) bunch of 4 mA in the center of a 200 ns wide dark gap, followed by the PPRE bunch,^{40,73} the standard multibunch train at 1 mA current per bunch separated by 2 ns, and slicing bunches deliver photons to the ultrafast timing experiments at the Femtoslicing facility.^{74,75} The PPRE bunch is utilized at BESSY II to provide quasi-single bunch light to timing users while operating a multi-bunch filling pattern. It has been realized by exciting the first synchrotron sideband of the horizontal betatron frequency to enlarge the beam horizontally with relatively small orbit perturbation and this bunch has typically a bunch current of 3 mA. Since the PPRE bunch has 1.2% (3/250 mA) of total beam current in the ring as well as a relatively larger beam size than the 1 mA standard multibunch, we anticipate observing the bunch as halo below the 10^{-2} level. This special bunch offers a unique opportunity for the

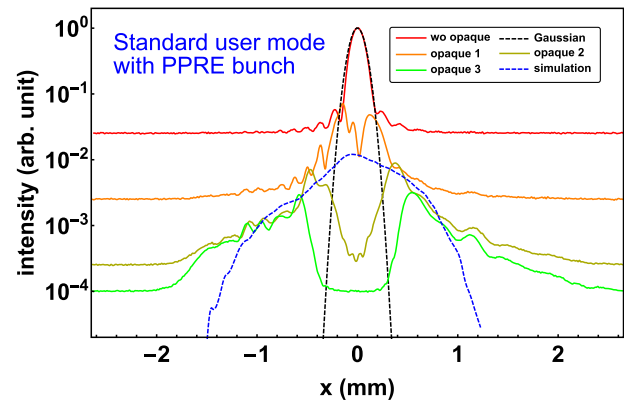


FIG. 8. Intensity distribution in the horizontal direction of beam halo with various opaque elements in the standard user mode of BESSY II with a beam current of 250 mA and a PPRE bunch current of 3 mA. The focal length of the objective, field, and relay lenses is 1.0, 0.5, and 0.25 m, respectively. The eyepieces with a magnification of 10 was used and all data are normalized by the exposure time of CCD camera.

coronagraph to verify the performance explicitly. In the experiment, various sizes of an opaque element were used to adjust the dynamic range of the monitor by removing the bright part of the beam. The full dynamic range is covered by using three different sized opaque elements.

As shown in Fig. 8, in the measurement without an opaque element, which is close to a direct source size monitor, the PPRE bunch is invisible owing to the background light. However, the PPRE bunch is clearly recognized when an appropriate opaque element is installed and the result shows that the particle distribution deviates greatly from the Gaussian distribution at the level of 10^{-2} contrast to the beam core. Furthermore, the result of numerical simulation using the Elegant code⁷⁶ shows qualitative agreement with the measurement.⁷³

In addition to the standard user mode discussed above, the BESSY II storage ring provides various sophisticated filling patterns such as a high-current single-bunch mode, a few bunch mode of 4 bunches, and a low- α multibunch hybrid mode for time-resolved studies. The low- α optics can be achieved by modifying a momentum compaction factor to smaller values by a special setting of the electron optics of the storage ring. Beam experiments were performed in the low- α mode without the PPRE bunch. Since the low- α beam size is larger than for the standard optics, the beam distribution is expected to be close to a Gaussian distribution. The result is shown in Fig. 9. The measured beam halo distribution is qualitatively close to Gaussian distribution for up to 10^{-3} contrast to the beam core. Due to background light, it is difficult to measure the practical halo distribution at 10^{-4} contrast to the beam core.

In general, halo particles are distributed on the shoulder of the high-intensity part of the beam, where relatively strong background light occurs in the coronagraph. This point makes the distinction between halo parts and background light difficult in the experiment. Therefore, it is worthy to measure the beam located off the section of the strong background light area in order to ensure the performance limitation of the beam halo monitor. This is feasible by TRIBs bunch,^{39,77,78} which is newly implemented at the BESSY II storage

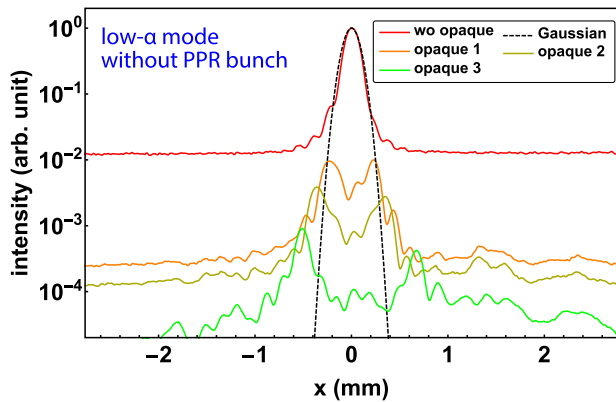


FIG. 9. Intensity distribution in the horizontal direction of beam halo with various opaque elements in the low- α mode. The other settings are identical to the ones in Fig. 8.

ring since 2017. This mode provides a special setting of the magnetic lattice for generating a second stable orbit, which closes after three revolutions. At each position in the storage ring, this yields three additional source spots. This special operation mode allows the beam separation in the horizontal plane as well as the manipulation option of bunch filling in the second orbit. The outer layering TRIBs bunch is placed beyond the background light. By using the

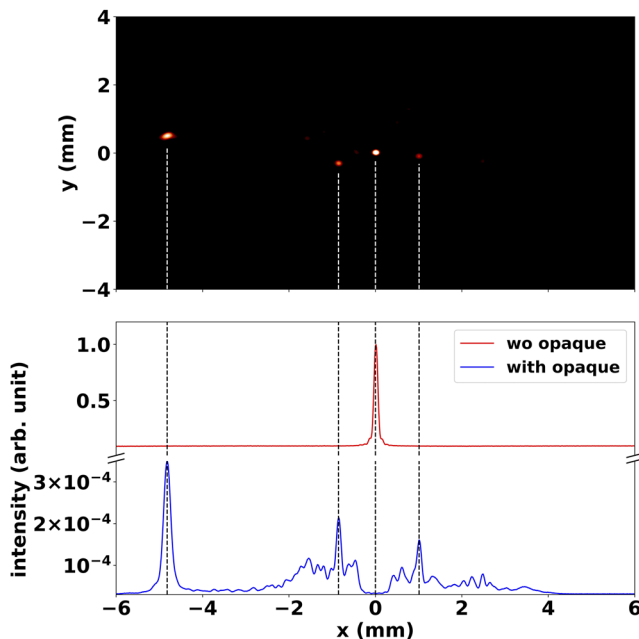


FIG. 10. Image of the core beam and diffused beams at the second stable (TRIBs) orbit (upper plot). The core beam image (without opaque elements) is rescaled by 5×10^{-4} and has been overlayed to the TRIBs beam profiles measured with an opaque element. In the lower plot, the projection of the intensity profile with the opaque element (blue curve) is shown together with the core beam profile obtained without the opaque element (red curve). The other settings are identical to the ones in Fig. 8.

halo monitor, we observed the diffused particles from the core orbit to the second stable orbit during commissioning of TRIBs. The measurement result of the diffused beam at the second stable orbit is shown in Fig. 10.

As shown in Fig. 10, the three TRIBs bunches are clearly distinguishable and the beam intensity is in good agreement with the values measured in a user beamline with comparable detectors. Particularly, it shows clearly that the coronagraph can achieve an extremely high signal-to-background ratio when the beam is far apart from the center of the image because the background light is suppressed by more than four orders of magnitude as suggested in Fig. 6. From this measurement, consequently, the halo monitor can be used potentially for continuous monitoring of the bunch in the second stable orbit during TRIBs operation.

IV. CONCLUSION

A design study and optimization of the coronagraph based halo monitor was performed to observe the halo distribution with $\sim 10^{-4}$ contrast to the beam core. The monitor is capable of performing halo measurements in the horizontal as well as vertical direction. The background diffraction pattern at the image plane of the relay lens has a relative peak intensity of about 3.0×10^{-5} with a radius of the Lyot stop of 5 mm. The background level can be mitigated further by adjusting the opening of the Lyot stop. The performance until now is limited by the polishing quality of the objective lens since the background noise produced by Mie-scattering effects owing to the digs and scratches on the lens surface produces a background level of 3×10^{-5} for a high-quality lens (10-5). The monitor has demonstrated its capability for measuring the transverse profile of special bunches in the BESSY II storage ring with a dynamic range of about 10^4 in experiments with electron beams. This monitor enables the non-invasive measurements of special bunches in the storage ring such as TRIBs and PPRE, which are newly developed for storage rings to serve timing users and high-flux users simultaneously. Recently, a new diagnostic platform that features visible-light output ports from two dipole beamlines of the BESSY II storage ring has been built for bunch-resolved diagnostics with sub-ps time resolution and micrometer spatial resolution^{49,79} so that the monitor is no longer available. However, we will rebuild the monitor at the new platform, which has an x-ray blocker to prevent thermal distortion of the front-end mirror.

ACKNOWLEDGMENTS

The authors wish to thank Professor T. Mitsuhashi from KEK for his valuable discussion. This work was supported by the German Bundesministerium für Bildung und Forschung, Land Berlin, and grants of the Helmholtz Association.

AUTHOR DECLARATIONS

Conflict of Interest

The authors have no conflicts to disclose.

DATA AVAILABILITY

The data that support the findings of this study are available from the corresponding authors upon reasonable request.

REFERENCES

- ¹M. Altarelli *et al.*, “The European X-ray free-electron laser,” Technical Report No. 97, DESY, 2006.
- ²K.-J. Kim, Y. Shvyd'ko, and S. Reiche, “A proposal for an X-ray free-electron laser oscillator with an energy-recovery linac,” *Phys. Rev. Lett.* **100**, 244802 (2008).
- ³P. Emma *et al.*, “Linear accelerator design for the LCLS-II FEL facility, in Proceedings of Free-Electron Laser Conference, Basel, 2014.
- ⁴J. Galayda *et al.*, “LCLS-II final design report,” Technical Report No. LCLSII-1.1-DR-0251-R0, SLAC, 2015.
- ⁵A. Halavanau, F.-J. Decker, C. Emma, J. Sheppard, and C. Pellegrini, “Very high brightness and power LCLS-II hard X-ray pulses,” *J. Synchrotron Radiat.* **26**, 635 (2019).
- ⁶W. Decking, S. Abeghyan, P. Abramian *et al.*, “A MHz-repetition-rate hard X-ray free-electron laser driven by a superconducting linear accelerator,” *Nat. Photonics* **14**, 391 (2020).
- ⁷Z. Zhang, A. S. Fisher, M. C. Hoffmann, B. Jacobson, P. S. Kirchmann, W.-S. Lee, A. Lindenberg, A. Marinelli, E. Nanni, R. Schoenlein, M. Qian, S. Sasaki, J. Xu, and Z. Huang, “A high-power, high-repetition-rate THz source for pump-probe experiments at Linac Coherent Light Source II,” *J. Synchrotron Radiat.* **27**, 890 (2020).
- ⁸R. Hajima, “Energy recovery linacs for light sources,” *Rev. Accel. Sci. Technol.* **03**, 121 (2010).
- ⁹I. Ben-Zvi, “Superconducting energy recovery linacs,” *Supercond. Sci. Technol.* **29**, 103002 (2016).
- ¹⁰D. Angal-Kalinin *et al.*, “PERLE. Powerful energy recovery linac for experiments. Conceptual design report,” *J. Phys. G: Nucl. Part. Phys.* **45**, 065003 (2018).
- ¹¹M. Akemoto *et al.*, “Construction and commissioning of the compact energy-recovery linac at KEK,” *Nucl. Instrum. Methods Phys. Res., Sect. A* **877**, 197 (2018).
- ¹²A. Jankowiak *et al.*, “BERLinPro: A compact demonstrator ERL for high current and low emittance beams,” in *Proceedings of LINAC'10* (JACoW Publishing, Tsukuba, 2010), p. 407.
- ¹³M. Abo-Bakr *et al.*, “The Berlin energy recovery linac project BERLinPro: Status, plans and future opportunities, in *Proceedings of ERL'19* (JACoW Publishing, Berlin, 2019), p. 8.
- ¹⁴J.-G. Hwang, T. Miyajima, Y. Honda, and E.-S. Kim, “Measurement of bunch length and temporal distribution using accelerating radio frequency cavity in low-emittance injector,” *Sci. Rep.* **10**, 18905 (2020).
- ¹⁵A. Bartnik *et al.*, “CBETA: First multipass superconducting linear accelerator with energy recovery,” *Phys. Rev. Lett.* **125**, 044803 (2020).
- ¹⁶R. C. York *et al.*, “FRIB: A new accelerator facility for the production of rare isotope beams,” in *Proceedings of SRF'09* (JACoW Publishing, Berlin, 2009), p. 888.
- ¹⁷D. Jeon *et al.*, “Design of the RAON accelerator systems,” *J. Korean Phys. Soc.* **65**, 1010 (2014).
- ¹⁸E.-S. Kim, J. Bahng, J.-G. Hwang, B.-H. Choi, H.-J. Kim, and D. Jeon, “Start-to-end simulations for beam dynamics in the RISP heavy-ion accelerator,” *Nucl. Instrum. Methods Phys. Res., Sect. A* **794**, 215 (2015).
- ¹⁹J.-G. Hwang, E.-S. Kim, H.-J. Kim, H. Jang, H. J. Kim, and D. Jeon, “Beam dynamics for high-power superconducting heavy-ion linear accelerator of RAON,” *IEEE Trans. Nucl. Sci.* **63**, 992 (2016).
- ²⁰W. Barth, K. Aulenbacher, M. Basten, F. Dziuba, V. Gettmann, M. Miski-Oglu, H. Podlech, and S. Yarmyshev, “A superconducting CW-LINAC for heavy ion acceleration at GSI,” *EPJ Web Conf.* **138**, 01026 (2017).
- ²¹W. Barth, K. Aulenbacher, M. Basten, M. Busch, F. Dziuba, V. Gettmann, M. Heilmann, T. Kürzeder, M. Miski-Oglu, H. Podlech, A. Rubin, A. Schnase, M. Schwarz, and S. Yarmyshev, “First heavy ion beam tests with a superconducting multipass CH cavity,” *Phys. Rev. Spec. Top. Accel. Beams* **21**, 020102 (2018).
- ²²P. N. Ostroumov, T. Maruta, S. Cogan, K. Fukushima, S. H. Kim, S. Lidia, F. Marti, A. S. Plastun, J. Wei, T. Yoshimoto, T. Zhang, and Q. Zhao, “Beam commissioning in the first superconducting segment of the Facility for Rare Isotope Beams,” *Phys. Rev. Spec. Top. Accel. Beams* **22**, 080101 (2019).
- ²³P. N. Ostroumov, S. Cogan, K. Fukushima, S. Lidia, T. Maruta, A. S. Plastun, J. Wei, J. Wong, T. Yoshimoto, and Q. Zhao, “Heavy ion beam acceleration in the first three cryomodules at the facility for rare isotope beams at michigan state university,” *Phys. Rev. Spec. Top. Accel. Beams* **22**, 040101 (2019).
- ²⁴T. Behnke, J. E. Brau, B. Foster, J. Fuster, and M. Harrison *et al.*, “The international linear collider technical design report: Volume 1: Executive summary, arXiv:1306.6327 [physics.acc-ph] (2013).
- ²⁵CLIC and CLICdp collaborations, Updated Baseline for a Staged Compact Linear Collider (CERN, 2016).
- ²⁶S. Michizono, “The international linear collider,” *Nat. Rev. Phys.* **1**, 244 (2019).
- ²⁷E. Sicking and R. Ström, “From precision physics to the energy Frontier with the Compact Linear Collider,” *Nat. Phys.* **16**, 386 (2020).
- ²⁸L. Evans and P. Bryant, “LHC machine,” *J. Instrum.* **3**, S08001 (2008).
- ²⁹M. Benedikt, D. Schulte, and F. Zimmermann, “Optimizing integrated luminosity of future hadron colliders,” *Phys. Rev. Spec. Top. Accel. Beams* **18**, 101002 (2015).
- ³⁰G. Arduini *et al.*, “High luminosity LHC: Challenges and plans,” *J. Instrum.* **11**, C12081 (2016).
- ³¹G. Apollinari, O. Bruening, T. Nakamoto, and L. Rossi, “High luminosity large hadron collider HL-LHC,” in *High-Luminosity Large Hadron Collider (HL-LHC): Preliminary Design Report* (CERN, 2015).
- ³²X. Lou, “The circular electron positron collider,” *Nat. Rev. Phys.* **1**, 232 (2019).
- ³³M. Benedikt, A. Blondel, P. Janot *et al.*, “Future circular colliders succeeding the LHC,” *Nat. Phys.* **16**, 402 (2020).
- ³⁴K. Wittenburg, “Beam halo and bunch purity monitoring,” in 2018 Proceedings of the CERN Accelerator School, Tuusula, 2018.
- ³⁵M. Abo-Bakr, W. Anders, R. Barday *et al.*, “Conceptual design report,” edited by B. Kuske, N. Paulick, A. Jankowiak, J. Knobloch (bERLinPro, Helmholtz-Zentrum, Berlin, 2015), https://www.helmholtz-berlin.de/media/media/grossgeraete/beschleunigerphysik/berlinpro_MAB/BPro_in_detail/Publications/bERLinPro_CDR.pdf.
- ³⁶See https://www.desy.de/~mpyflo/Astra_documentation/ for OPAL website.
- ³⁷J.-G. Hwang and J. Kuszynski, “Coronagraph based beam halo monitor development for bERLinPro,” in *Proceedings of IPAC'17* (JACoW Publishing, Copenhagen, 2017), p. 355.
- ³⁸P. Goslawski, F. Andreas, F. Armbrorst, T. Atkinson, J. Feikes, A. Jankowiak, J. Li, T. Mertens, M. Ries, A. Schällicke, G. Schiwietz, and G. Wüstefeld, “Two orbit operation at Bessy II: During a user test week,” in *Proceedings of IPAC'19* (JACoW Publishing, Melbourne, 2019), p. 3419.
- ³⁹K. Holldack, C. Schüssler-Langeheine, P. Goslawski, N. Pontius, T. Kachel, F. Armbrorst, M. Ries, A. Schällicke, M. Scheer, W. Frentrup, and J. Bahrdr, “Flipping the helicity of X-rays from an undulator at unprecedented speed,” *Commun. Phys.* **3**, 61 (2020).
- ⁴⁰K. Holldack, R. Ovsyannikov, P. Kuske, R. Müller, A. Schällicke, M. Scheer, M. Gorgoi, D. Kühn, T. Leitner, S. Svensson, N. Mårtensson, and A. Föhlich, “Single bunch X-ray pulses on demand from a multi-bunch synchrotron radiation source,” *Nat. Commun.* **5**, 4010 (2014).
- ⁴¹T. Mitsuhashi, “Beam profile and size measurement by SR interferometer,” in *Beam Measurement*, edited by S. Kurokawa *et al.* (World Scientific, 1999), pp. 399–427.
- ⁴²K. Holldack, J. Feikes, and W. B. Peatman, “Source size and emittance monitoring on BESSY II,” *Nucl. Instrum. Methods Phys. Res., Sect. A* **467–468**, 235 (2001).
- ⁴³T. Naito and T. Mitsuhashi, “Very small beam-size measurement by a reflective synchrotron radiation interferometer,” *Phys. Rev. Spec. Top. Accel. Beams* **9**, 122802 (2006).
- ⁴⁴C. Thomas, G. Rehm, I. Martin, and R. Bartolini, “X-ray pinhole camera resolution and emittance measurement,” *Phys. Rev. Spec. Top. Accel. Beams* **13**, 022805 (2010).
- ⁴⁵E. Gütlich, P. Forck, W. Ensinger, and B. Walasek-Höhne, “Scintillation screen investigations for high-current ion beams,” *IEEE Trans. Nucl. Sci.* **57**, 1414 (2010).
- ⁴⁶G. Kube, S. Bajt, A. P. Potylitsyn, L. G. Sukhikh, A. V. Vukolov, I. A. Artyukov, and W. Lauth, “Transverse beam profile imaging of few-micrometer beam sizes based on a scintillator screen,” in *Proceedings of IBIC'15* (JACoW Publishing, Melbourne, 2015), p. 330.

- ⁴⁷J.-G. Hwang *et al.*, “Effects of mirror distortion by thermal deformation in an interferometry beam size monitor system at PLS-II,” *Nucl. Instrum. Methods Phys. Res., Sect. A* **833**, 156 (2016).
- ⁴⁸A. Potylitsyn, L. Sukhikh, T. Gusvitskii, G. Kube, and A. Novokshonov, “Image of the transverse bunch profile via coherent optical transition radiation,” *Phys. Rev. Accel. Beams* **23**, 042804 (2020).
- ⁴⁹G. Schiwietz, J.-G. Hwang, A. Jankowiak, M. Koopmans, and M. Ries, “Bunch-resolved diagnostics for a future electron-storage ring,” *Nucl. Instrum. Methods Phys. Res., Sect. A* **990**, 164992 (2021).
- ⁵⁰T. Mitsuhashi, “Beam halo observation by coronagraph,” in *Proceedings of DIPAC’05* (JACoW Publishing, Lyon, 2005), p. 7.
- ⁵¹T. Mitsuhashi, E. Bravin, O. R. Jones, F. Roncarolo, and H. Schmickler, “Design of coronagraph for the observation of beam halo at LHC,” in *Proceedings of IBIC’15* (JACoW Publishing, Melbourne, 2015), p. 288.
- ⁵²T. Mitsuhashi, E. Bravin, F. Roncarolo, and G. Trad, “First observation of the LHC beam halo using a synchrotron radiation coronagraph,” in *Proceedings of IPAC’17* (JACoW Publishing, Copenhagen, 2017), p. 1244.
- ⁵³J.-G. Hwang and J. Kuszynski, “First prototype of a coronagraph-based halo monitor for bERLinPro,” in *Proceedings of IBIC’18* (JACoW Publishing, Shanghai, 2018), p. WEPB03.
- ⁵⁴H. Aoyagi *et al.*, “Pulse-mode measurement of electron beam halo using diamond-based detector,” *Phys. Rev. Spec. Top. Accel. Beams* **15**, 022801 (2012).
- ⁵⁵T. Lensch, S. Liu, and M. Scholz, “The European XFEL wire scanner system,” in *Proceedings of IBIC’18* (JACoW Publishing, Shanghai, 2018), p. 498.
- ⁵⁶M. Moszyński *et al.*, “Properties of the YAG:Ce scintillator,” *Nucl. Inst. and Meth. A* **345**, 461 (1994).
- ⁵⁷T. Naito and T. Mitsuhashi, “Beam halo measurement utilizing YAG:Ce screen,” in *Proceedings of IBIC’15* (JACoW Publishing, Melbourne, 2015), p. 373.
- ⁵⁸R. Yang, P. Bambade, S. Wallon, T. Naito, A. Aryshev, N. Terunuma, and M. Bergamaschi, “Development of a YAG/OTR monitor for beam halo diagnostics,” *Proceedings of IBIC’18* (JACoW Publishing, Shanghai, 2018), p. 429.
- ⁵⁹S. Liu, F. Bogard, P. Corneise, A. Faus-Golfe, N. Fuster-Martínez, E. Griesmayer, H. Guler, V. Kubytskyi, C. Sylvia, T. Tauchi, N. Terunuma, and P. Bambade, “In vacuum diamond sensor scanner for beam halo measurements in the beam line at the KEK Accelerator Test Facility,” *Nucl. Instrum. Methods Phys. Res., Sect. A* **832**, 231 (2016).
- ⁶⁰C. P. Welsch, E. Bravin, B. Burel, T. Lefèvre, T. Chapman, and M. J. Pilon, “Alternative techniques for beam halo measurements,” *Meas. Sci. Technol.* **17**, 2035 (2006).
- ⁶¹C. P. Welsch *et al.*, “High dynamic range beam profile measurements,” *2006 10th European Particle Accelerator Conference (EPAC)* (e-proceedings JACoW, Edinburgh, 2006), pp. 1217–1219.
- ⁶²H. D. Zhang, R. B. Fiorito, A. G. Shkvarunets, R. A. Kishek, and C. P. Welsch, “Beam halo imaging with a digital optical mask,” *Phys. Rev. Spec. Top. Accel. Beams* **15**, 072803 (2012).
- ⁶³A. Lipson, S. G. Lipson, and H. Lipson, *Optical Physics*, 4th ed. (Cambridge University Press, 2011).
- ⁶⁴M. Born and E. Wolf, *Principles of Optics: Electromagnetic Theory of Propagation, Interference and Diffraction of Light*, 7th ed. (Cambridge University Press, Cambridge, 1999).
- ⁶⁵N. V. Smolyakov, “Wave-optical properties of synchrotron radiation,” *Nucl. Instrum. Methods Phys. Res., Sect. A* **405**, 235 (1998).
- ⁶⁶R. Rougeot, R. Flamary, D. Galano, and C. Aime, “Performance of the hybrid externally occulted Lyot solar coronagraph,” *Astron. Astrophys.* **599**, A2 (2017).
- ⁶⁷C. F. Bohren and D. R. Huffman, *Absorption and Scattering of Light by Small Particles*, 1st ed. (Wiley VCH, 1998).
- ⁶⁸U.S. Military Performance Specification. General specification governing the manufacturing, assembly, and inspection of Optical Components for Fire Control Instruments. Mil-PRF-13830B, 1997.
- ⁶⁹T. M. Mitsuhashi, “Analysis of Mie scattering noise of objective lens in coronagraph for halo measurement,” in *Proceedings of IBIC’17* (JACoW Publishing, MI, 2017), p. 369.
- ⁷⁰R. Rougeot, R. Flamary, D. Mary, and C. Aime, “Influence of surface roughness on diffraction in the externally occulted Lyot solar coronagraph,” *Astron. Astrophys.* **626**, A1 (2019).
- ⁷¹M. Koopmans, P. Goslawski, J.-G. Hwang, M. Ries, M. Ruprecht, and A. Schällicke, “Status of a double slit interferometer for transverse beam size measurements at BESSY II,” in *Proceedings of IPAC’17* (JACoW Publishing, Copenhagen, 2017), p. 149.
- ⁷²M. Koopmans, P. Goslawski, J.-G. Hwang, A. Jankowiak, M. Ries, A. Schällicke, and G. Schiwietz, “Applications of the interferometric beam size monitor at BESSY II,” in *Proceedings of IPAC’18* (JACoW Publishing, Vancouver, 2018), p. 2103.
- ⁷³J.-G. Hwang, M. Koopmans, M. Ries, A. Schällicke, and R. Müller, “Analytical and numerical analysis of longitudinally coupled transverse dynamics of Pulse Picking by Resonant Excitation in storage rings serving timing and high-flux users simultaneously,” *Nucl. Instrum. Methods Phys. Res., Sect. A* **940**, 387 (2019).
- ⁷⁴K. Holldack, T. Kachel, S. Khan, R. Mitzner, and T. Quast, “Characterization of laser-electron interaction at the BESSY II femtoslicing source,” *Phys. Rev. Spec. Top. Accel. Beams* **8**, 040704 (2005).
- ⁷⁵S. Khan, K. Holldack, T. Kachel, R. Mitzner, and T. Quast, “Femtosecond undulator radiation from sliced electron bunches,” *Phys. Rev. Lett.* **97**, 074801 (2006).
- ⁷⁶M. Borland, “Elegant: A flexible SDDS-compliant code for accelerator simulation,” *Advanced Photon Source LS 287*, 2000.
- ⁷⁷P. Goslawski *et al.*, “Resonance island experiments at BESSY II for user applications,” in *Proceedings of IPAC’16* (JACoW Publishing, Busan, 2016), pp. 3427–3430.
- ⁷⁸P. Goslawski *et al.*, “Transverse resonance island buckets as bunch separation scheme,” in *Proceedings of IPAC’17* (JACoW Publishing, Copenhagen, 2017), pp. 3059–3062.
- ⁷⁹G. Schiwietz, J.-G. Hwang, M. Koopmans, M. Ries, and A. Schällicke, “Development of the electron-beam diagnostics for the future BESSY-VSR storage ring,” *IOP Conf. Ser.: J. Phys.: Conf. Ser.* **1067**, 072005 (2018).